Mathematical Biology

Model of pattern formation in marsh ecosystems with nonlocal interactions

Sofya Zaytseva[1,3] · Junping Shi[2] · Leah B. Shaw[2]

Abstract

Smooth cordgrass *Spartina alterniflora* is a grass species commonly found in tidal marshes. It is an ecosystem engineer, capable of modifying the structure of its surrounding environment through various feedbacks. The scale-dependent feedback between marsh grass and sediment volume is particularly of interest. Locally, the marsh vegetation attenuates hydrodynamic energy, enhancing sediment accretion and promoting further vegetation growth. In turn, the diverted water flow promotes the formation of erosion troughs over longer distances. This scale-dependent feedback may explain the characteristic spatially varying marsh shoreline, commonly observed in nature. We propose a mathematical framework to model grass–sediment dynamics as a system of reaction–diffusion equations with an additional nonlocal term quantifying the short-range positive and long-range negative grass–sediment interactions. We use a Mexican-hat kernel function to model this scale-dependent feedback. We perform a steady state biharmonic approximation of our system and derive conditions for the emergence of spatial patterns, corresponding to a spatially varying marsh shoreline. We find that the emergence of such patterns depends on the spatial scale and strength of the scale-dependent feedback, specified by the width and amplitude of the Mexican-hat kernel function.

✉ Sofya Zaytseva
  szaytseva@uga.edu

1   Department of Applied Science, William & Mary, Williamsburg, VA 23187-8795, USA

2   Department of Mathematics, William & Mary, Williamsburg, VA 23187-8795, USA

3   Present Address: Department of Mathematics, University of Georgia, Athens, GA 30602, USA

1 Introduction

Tidal marshes are among the richest and most productive ecosystems, supporting a variety of wildlife, serving as storm and erosion buffers, and playing an important role in improving water quality (Perry and Atkinson 2009; Fagherazzi et al. 2013; Fagherazzi 2014). The global loss of these ecosystems in the recent decades has motivated much research to understand their dynamics and aid in their restoration and management (Deegan et al. 2012; Priestas et al. 2015). Marsh evolution is dynamic and complex, combining various biological and morphological processes happening not only in the marsh itself, but also in the tidal flat that borders it. As a result of these forces and interactions, a sharp scarp separating the marsh and tidal flat becomes a characteristic feature (Mariotti and Fagherazzi 2010). The processes that take place on this scarp (i.e., marsh edge) influence whether the marsh recedes or expands (Tonelli et al. 2010). Various configurations of the marsh edge can be observed in nature, ranging from a uniform to a more jaggedy, sinusoidal shoreline (Fig. 1). While previous ecogeomorphic models have carefully considered the effects of sea-level rise, marsh vegetation colonization, wave activity, sediment fluxes, and underlying hydrodynamics (Mariotti and Fagherazzi 2010; Tonelli et al. 2010; Fagherazzi et al. 2012; Schile 2014), most of these have been numerical, computationally intensive models. We propose a simpler, phenomenological model to describe the large-scale evolution of the marsh in the horizontal direction in terms of two-way interactions between marsh vegetation and sedimentation. In particular, we are interested in the scale-dependent feedback present between marsh vegetation and sedimentation and whether this scale-dependent feedback can explain the spatially varying marsh shoreline, observed in nature.

Scale-dependent feedbacks are characterized by the presence of positive and negative interactions that happen at different spatial scales. In particular, scale-dependent feedbacks involving long-range negative interactions and short-range positive interactions are thought to be crucial for pattern development (Gierer and Meinhardt 1972; Green and Sharpe 2015; Hiscock and Megason 2015), explaining spatially varying patterns in chemical (Castets et al. 1990; Rovinsky and Menzinger 1993), biological (Nakamasu et al. 2009; Raspopovic et al. 2014) and ecological systems (Rietkerk and van de Koppel 2008). In ecological systems, such scale-dependent feedbacks are thought to explain patterns in arid savannas, mussel beds, coral and oyster reefs, mudflats and other ecosystems (Rietkerk and van de Koppel 2008; van der Heide et al. 2012; Dibner et al. 2015; de Jager et al. 2017; Pringle and Tarnita 2017; Barbier et al. 2008). Previously, we proposed a mathematical framework to investigate the evolution of the marsh edge as a result of scale-dependent interactions between sedimentation dynamics and two common marsh species, ribbed mussels (*Geukensia demissa*) and smooth cordgrass (*Spartina alterniflora*) (Zaytseva et al. 2018), whose facilitatory nature and positive feedbacks have a significant effect on marsh development and proliferation (Bertness 1984; Bertness and Grosholz 1985; Watt et al. 2010; Altieri et al. 2007). While mussels are commonly found in tidal marshes, that is not always the case. Since we are interested in the marsh edge dynamics in the absence of mussels, in this paper we focus on the related model without the mussel population. The goal is to understand which conditions lead to a spatially varying marsh shoreline (Fig. 1a)

Fig. 1 **a** Self-organization on the marsh edge in the York River, a tributary of the Chesapeake Bay. *Credit*: Romuald N. Lipcius, Chris Neill. **b** Uniform marsh edge. *Credit*: NOAA National Ocean Service (color figure online)

versus a spatially uniform marsh shoreline (Fig. 1b) and what may be the implications of this spatial heterogeneity.

In general, there are three classes of deterministic models that explain pattern formation as a result of scale-dependent feedbacks: Turing-style activator–inhibitor models, kernel-based models and differential flow models (Borgogno et al. 2009). In Turing-style activator–inhibitor models, the pattern formation arises as a result of differences in the diffusion coefficients of the activator and inhibitor species (Turing 1952; White 1998; Parshad et al. 2014). Kernel-based models are typically integro-differential equations where the pattern formation arises from the spatial interactions modeled using a kernel function, describing the nature of the short-range and long-range interactions (Britton 1990; Gourley et al. 2001; Murray 2001; Billingham 2003; Ninomiya et al. 2017). This kernel-based approach is a common feature in neural models (Amari 1977), and has also been used in models of vegetation patterns in arid and semi-arid climates (D'Odorico et al. 2006; Borgogno et al. 2009; Merchant and Nagata 2011; Martínez-García et al. 2013, 2014; Martínez-García and Lopez 2018). Finally, differential flow models are similar to Turing models but the pattern formation now arises not just from the differences in diffusion coefficients, but also from the differences in the flow rates of the species, reflected in the additional advection terms (Rovinsky and Menzinger 1993; Siero et al. 2015; Klausmeier 1999).

The model we propose here combines elements of both the Turing-model and the kernel-based model and includes both diffusion terms and a kernel function that describes the short-range and long-range interactions between marsh grass and sediment volume. On a local scale, marsh grass attenuates hydrodynamic energy, enhancing sediment accretion and promoting further vegetation growth while the diverted water flow promotes formation of erosion troughs over longer distances (Bouma et al. 2007; Balke et al. 2012; Schwarz et al. 2015). We model this scale-dependent feedback using a Mexican-hat kernel function that quantifies the strength of positive and negative feedbacks neighboring individuals exert on each other (Fuentes et al. 2003; D'Odorico et al. 2006; Borgogno et al. 2009; Siebert and Schöll 2015). Similar kernel-based approaches have been used to model nonlocal interactions in the context of predator–prey and competition dynamics (Merchant and Nagata 2011; Bayliss and Volpert 2015; Banerjee and Volpert 2016). The interactions in our system are mostly cooperative and the impact of nonlocal interactions in such systems have not been studied in depth. Given the importance of facilitation in ecosystem dynamics (Bertness and Callaway 1994; Halpern et al. 2007; Silliman et al. 2015; He et al. 2013), it therefore becomes imperative to study nonlocal interactions in cooperative systems. In addition, cooperative systems are likely to display bistable dynamics and the phenomenon of hysteresis (Kéfi et al. 2016; van de Koppel et al. 2001). This makes such systems especially prone to collapsing to an irreversible state as environmental conditions gradually worsen and a tipping point is reached (Dakos et al. 2011; Kéfi et al. 2014, 2016). Pattern formation has previously been suggested as a possible coping mechanism, allowing such systems to escape degradation past their tipping point (Chen et al. 2015). Due to the reported degradation of tidal marsh habitats around the world, the study of pattern formation in these systems becomes particularly important and can provide more insight into the possible pattern forming mechanism and its implication for the system's resilience and adaptation to environmental changes.

Our paper is organized as follows: in Sect. 2, we introduce the nonlocal reaction–diffusion model and the background from ecological literature. Section 3 includes analysis and simulation results. By approximating our model using a steady state biharmonic approximation, we are able to derive conditions for the emergence of spatial patterns in our system. We then use numerical simulations to confirm our theoretical findings. Some concluding remarks are made in Sect. 4.

2 Model

We consider the two-way interactions between marsh grass and sediment (Fig. 2). Marsh grass binds sediment, stabilizes the marsh edge and attenuates wave energy, helping to mitigate effects of erosion (Gleason et al. 1979; Gedan et al. 2011; Ysebaert et al. 2011; Möller et al. 2014). As a consequence of reduced erosion, the increased sediment levels promote vegetation growth by decreasing tidal currents (Nyman et al. 1993; van de Koppel et al. 2005b). Along with these local interactions, there is a non-local interaction that occurs between marsh vegetation and sediment (van Wesenbeeck et al. 2008; Schwarz et al. 2015; Bouma et al. 2009; Van Hulzen et al. 2007). Over short distances, marsh vegetation enhances sediment accretion through the attenuation
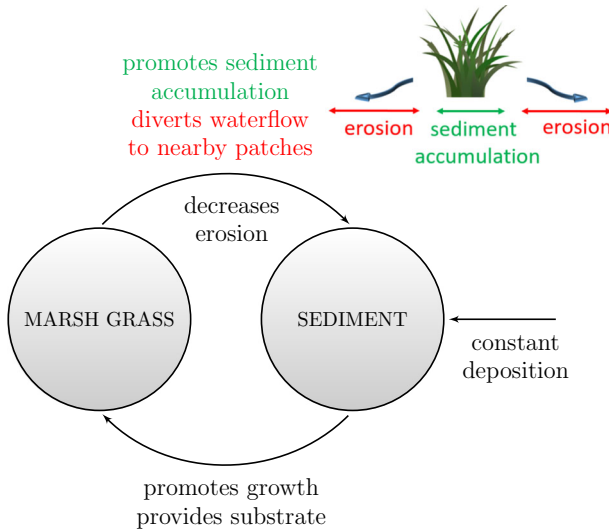
Fig. 2 Diagram of grass–sediment interactions adapted from (Bertness 1984) (color figure online)

of hydrodynamic energy, contributing to short-range activation. However, as the water gets diverted to the surrounding areas, those areas erode more quickly, contributing to long-range inhibition (Bouma et al. 2007; Balke et al. 2012; Bouma et al. 2013; Fagherazzi et al. 2013; Fagherazzi 2014).

Incorporating all the above mentioned interactions, we obtain the following system:

$$
\begin{cases}
\partial_\tau \hat{G} = \hat{D}_{\hat{G}} \partial_x^2 \hat{G} + \underbrace{\hat{G}\left(\hat{F}(\hat{S}) - c\hat{G}\right)}_{\text{Logistic growth}}, & x \in \mathbb{R}, \quad \tau > 0, \\
\partial_\tau \hat{S} = \hat{D}_{\hat{S}} \partial_x^2 \hat{S} + \underbrace{\eta}_{\text{Deposition}} - \underbrace{\hat{S}\hat{L}(\hat{G})}_{\text{Erosion}} + \underbrace{\hat{\lambda}\hat{S} \int_{-\infty}^{\infty} P(x')\hat{G}(x-x')dx'}_{\text{Nonlocal deposition/erosion}}, & x \in \mathbb{R}, \quad \tau > 0, \quad (2.1) \\
\hat{G}(x,0) = \hat{G}_0(x,0) \geq 0, \quad \hat{S}(x,0) = \hat{S}_0(x,0) \geq 0, & x \in \mathbb{R}.
\end{cases}
$$

where

$$
\hat{F}(\hat{S}) = \frac{p^*(\hat{S} - l_1)}{\hat{S} + l_1^*}, \quad \hat{L}(\hat{G}) = \frac{\psi(\hat{G} + k_s g)}{\hat{G} + k_s},
$$

with

$$
p^*, c, l_1, l_1^*, \psi, k_s, g, \eta, \hat{\lambda} \geq 0.
$$

We consider the change in grass shoot density $\hat{G}(x,t)$ (shoots/m^2) and sediment height $\hat{S}(x,t)$ (m) on an infinite domain with $x \in \mathbb{R}$, which represents the one-dimensional horizontal cross-section of the marsh edge (see Fig. 3a). We assume logistic growth for the grass equation and make an adjustment for the obligatory nature of grass–sediment interactions. This is reflected in the functional form of $\hat{F}(\hat{S})$, which describes the intrinsic growth rate of grass as a function of sediment height. A biologically realistic assumption is that a certain minimum amount of sediment/soil is necessary
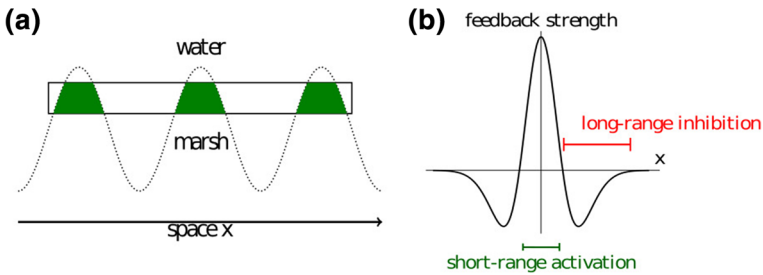
Fig. 3 Illustration of **a** the cross-section of marsh edge used to model the marsh dynamics, **b** Mexican-hat kernel and scale-dependent feedback adapted from (Rietkerk and van de Koppel 2008) (color figure online)

for plants to grow. Therefore, the term $\hat{F}(\hat{S})$ ensures that for sediment heights less than some threshold l_1, grass cannot persist and the growth rate becomes negative. For the sediment equation, we include the baseline sediment deposition η (van de Koppel et al. 2005a; Liu et al. 2012, 2014). The erosion term $\hat{L}(\hat{G})$ is assumed to be a decreasing function of grass density $\hat{G}$, decaying to some non-zero erosion rate ψ for very large grass densities. The parameter $g > 1$ controls the erosion intensity with the erosion rate ψg corresponding to the maximum erosion rate in the total absence of grass. This is consistent with previous findings where erosion was greatest in the absence of grass (Mariotti and Fagherazzi 2010; Silliman et al. 2012). This choice of the function $\hat{L}(\hat{G})$ ensures the non-negativity of the erosion rate and accounts for a biologically realistic scenario of a persistent baseline erosion rate. In addition, each equation also includes a diffusion term to quantify spread along the shoreline with diffusion coefficients $\hat{D}_{\hat{G}}$ and $\hat{D}_{\hat{S}}$. To model the scale-dependent interactions, we use a convolution term with a Mexican-hat kernel function $P(x)$:

$$P(x) = \frac{1}{\sqrt{2\pi}} \left[\frac{1}{\sigma_1} \exp\left(-\frac{x^2}{2\sigma_1^2}\right) - \frac{1}{\sigma_2} \exp\left(-\frac{x^2}{2\sigma_2^2}\right) \right], \quad \sigma_1 < \sigma_2. \quad (2.2)$$

The choice of the kernel function is appropriate given the nature of the scale-dependent feedback with short-range positive interactions and long-range negative interactions (Fig. 3b). There are three main parameters that control the shape of the kernel: $\hat{\lambda}$, which modulates the amplitude and variances σ_1^2 and σ_2^2, which specify the scale of the excitatory and inhibitory interactions, respectively. Further, the kernel function $P(x)$ is symmetric and satisfies the following property:

$$\int_{-\infty}^{\infty} P(x)dx = 0. \quad (2.3)$$

For mathematical simplification, we non-dimensionalize system (2.1) by using the following rescaling:

$$t = p^*\tau, \quad G = \frac{c}{p^*}\hat{G}, \quad S = \frac{\psi g}{\eta}\hat{S}.$$

Then the original system (2.1) becomes:

$$
\begin{cases}
\partial_t G = D_G \partial_x^2 G + G\big(F(S) - G\big), & x \in \mathbb{R}, t > 0, \\
\partial_t S = D_S \partial_x^2 S + \phi\big(-L(G)S + 1\big) + \lambda S \int_{-\infty}^{\infty} P(x')G(x - x')dx', & x \in \mathbb{R}, t > 0, \\
G(x, 0) = G_0(x, 0) \geq 0, \quad S(x, 0) = S_0(x, 0) \geq 0, & x \in \mathbb{R}.
\end{cases}
\tag{2.4}
$$

with

$$
F(S) = \frac{S - e_1}{S + p_1}, \quad L(G) = \frac{\delta G + e_3}{G + e_3},
\tag{2.5}
$$

and $P(x)$ still defined as before. The new parameters are all positive with the following rescaling:

$$
e_1 = \frac{\psi g l_1}{\eta}, \quad p_1 = \frac{\psi g l_1^*}{\eta}, \quad e_3 = \frac{k_s c}{p^*}, \quad \delta = \frac{1}{g}
$$

$$
\phi = \frac{\psi g}{p^*}, \quad D_G = \frac{\hat{D}_G}{p^*}, \quad D_S = \frac{\hat{D}_S}{p^*}, \quad \lambda = \frac{\lambda}{c}.
$$

Not only does this rescaling simplify the notation, but it also allows for an easier interpretation of the functional forms of $F(S)$ and $L(G)$ (see Fig. 10 in "Appendix" section). The scaled intrinsic growth rate of grass is now between 0 and 1, and we can think of the threshold e_1 as the minimum amount of sediment necessary for the persistence of grass. Similarly, the erosion term given by $L(G)$ is scaled to be between δ and 1 for ease of interpretation.

3 Results

In classic Turing models, spatially patterned solutions result from symmetry-breaking instability in which an otherwise stable spatially uniform steady state can become destabilized by the addition of diffusion and lead to the emergence of spatial patterns. The condition for the emergence of spatial patterns is contingent on the idea that the species in the model diffuse at significantly different rates, with the activator species diffusing much more slowly than the inhibitor species. The conditions for such a Turing-instability can be derived by performing a linear stability analysis around the positive steady state to obtain conditions under which the addition of diffusion acts to destabilize the system. Our model differs from the classic Turing model in that it lacks the classic activator–inhibitor dynamics and includes an additional kernel function term that models the scale-dependent feedback between grass and sediment volume. Assuming that the kernel function has a limited effect at relatively large distances, we can perform a biharmonic approximation of our system and decompose the integral term into two terms involving just partial derivatives, corresponding to short-range positive interactions and long-range negative interactions. We can then perform a linear stability analysis around the positive steady state and derive conditions under which this state is destabilized and leads to the emergence of a spatially periodic solution.

Therefore, we first consider the spatially independent dynamics of our model and derive conditions under which the positive steady state is stable in the corresponding system of ODEs and then use these results to understand the spatial dynamics of the full model.

3.1 Spatially homogeneous model

Let's assume that G and S do not vary and are spatially constant. Then, we can use the property in (2.3) and drop both the diffusion and integral terms. In this way, we are left with the following spatially independent system:

$$\begin{cases} \frac{dG}{dt} = G\Big(F(S) - G\Big), & t > 0, \\ \frac{dS}{dt} = \phi(-L(G)S + 1), & t > 0. \end{cases} \tag{3.1}$$

We look for spatially uniform steady states (G^*, S^*) of (3.1) which satisfy $\frac{dG}{dt} = 0$ and $\frac{dS}{dt} = 0$. There are two such types of steady states: the degraded (grass-free) state $E_S = (0, 1)$ and the coexistence state $E_{GS} = (G^*, \frac{1}{L(G^*)})$ with both grass and sediment present, where G^* satisfies $G = F(\frac{1}{L(G)})$. Since we are interested in physically realistic positive steady states, the coexistence state E_{GS} exists if and only if $\frac{1}{L(G^*)} > e_1$.

We first consider the degraded state $E_S = (0, 1)$ and its stability. This result is summarized below.

Proposition 3.1 *The degraded steady state $E_S = (0, 1)$ is locally asymptotically stable with respect to (3.1) if $e_1 > 1$ and is unstable with respect to (3.1) if $e_1 < 1$.*

Proof The Jacobian matrix **J** of (3.1) evaluated at $E_S = (0, 1)$ is given by:

$$\mathbf{J}_{E_S} = \begin{bmatrix} F(1) & 0 \\ -\phi\frac{dL}{dG} & -\phi L(0) \end{bmatrix}.$$

The two corresponding eigenvalues are $\lambda_1 = F(1) = \frac{1-e_1}{1+p_1}$ and $\lambda_2 = -\phi L(0) = -\phi$. It is clear that λ_2 is always negative. Further, $\lambda_1 = \frac{1-e_1}{p_1+1}$ is negative for $e_1 > 1$. Therefore, the steady state E_S is locally asymptotically stable for $e_1 > 1$ and unstable for $e_1 < 1$. □

The parameter e_1 is the minimal steady state sediment elevation needed for the persistence of grass. For the trivial steady state $E_S = (0, 1)$, as long as $e_1 > 1$, its value will exceed the steady state value of sediment, leading to a negative growth rate for grass and a stable trivial state.

We now consider the positive coexistence steady state $E_{GS} = \left(G^*, \frac{1}{L(G^*)}\right)$ where G^* satisfies $G = F\left(\frac{1}{L(G)}\right)$ and obtain the following theorem:

Theorem 3.2 *Suppose that $p_1, e_1, e_3, \phi > 0$ and $0 < \delta < 1$. Let*

$$A = 1 + p_1\delta, \quad B = -1 + e_3 + p_1 e_3. \tag{3.2}$$

1. (**Case I**) *If $B + \delta < 0$, then there exists a saddle-node bifurcation point $e_1 = e_1^* > 1$ such that (3.1) has one positive steady state $(G_+^*, \frac{1}{L(G_+^*)})$ for $0 < e_1 \le 1$ and $e_1 = e_1^*$, two positive steady states $(G_\pm^*, \frac{1}{L(G_\pm)})$ for $1 < e_1 < e_1^*$, and no positive steady state for $e_1 > e_1^*$. The bifurcation point e_1^* is defined as follows:*

$$e_1^* = \frac{2e_3 A(\delta^2 + B\delta - Ae_3) + (2Ae_3 - B\delta)\sqrt{A^2 e_3^2 - Ae_3\delta(B+\delta)}}{\delta^2 \sqrt{A^2 e_3^2 - Ae_3\delta(B+\delta)}}. \tag{3.3}$$

2. (**Case II**) *If $B + \delta \ge 0$, then there exists a unique positive steady state $(G_+^*, \frac{1}{L(G_+^*)})$ for all $0 < e_1 < 1$, and no positive steady state for $e_1 \ge 1$.*

Proof We can rewrite $G = F(\frac{1}{L(G)})$ as

$$G = \frac{\frac{1}{L(G)} - e_1}{\frac{1}{L(G)} + p_1}$$

$$\implies e_1 = \frac{1 - G}{L(G)} - p_1 G$$

$$\implies e_1 = \frac{e_3 - BG - AG^2}{G\delta + e_3} := K(G), \tag{3.4}$$

where A and B are defined as in (3.2). The function $K(G)$ from (3.4) crosses the horizontal axis at

$$G_K^\pm = \frac{-B \pm \sqrt{B^2 + 4e_3 A}}{2A}. \tag{3.5}$$

Since $A \ge 0$, the roots in (3.5) have to be of opposite sign. Therefore, the graph of $K(G)$ has one positive and one negative root. Note that the vertical asymptote of $K(G)$ is irrelevant as it is located where G is negative and outside of the physically realistic range.

Differentiating $K(G)$ in (3.4) with respect to G yields:

$$K'(G) = \frac{-B - 2AG - \delta K(G)}{\delta G + e_3} = \frac{-AG(2e_3 + \delta G) - e_3(B + \delta)}{(\delta G + e_3)^2}$$

$$= \frac{-L(G) - L'(G)(1 - G)}{L(G)^2} - p_1, \tag{3.6}$$

(a)   **(b)**
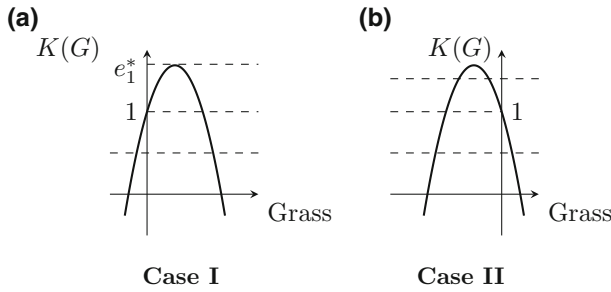
Case I   **Case II**

Fig. 4 Schematics representations of parameter regimes for the positive coexistence steady state E_{GS}. Case I corresponds to the scenario where marsh vegetation is very efficient at reducing erosion and $e_3 < \frac{1-\delta}{1+p_1}$. The horizontal values represent various values of e_1. We see that for $e_1 > 1$, we have two real, positive steady states. They eventually collide and disappear in a saddle node bifurcation e_1^*. For Case II, the case of less efficient vegetation, we see that for $e_1 \geq 1$, there are no positive steady states and for $e_1 < 1$, there is only one

and

$$K(0) = 1, \quad K'(0) = \frac{-(B+\delta)}{e_3}, \tag{3.7}$$

Further, we can set $K'(G) = 0$ to obtain the maximum and minimum points of the function:

$$\tilde{G}_\pm = \frac{-e_3 \pm \sqrt{e_3^2 - \frac{e_3\delta(B+\delta)}{A}}}{\delta}. \tag{3.8}$$

We then have two cases arising depending on the sign of $K'(0)$ in (3.7) (Fig. 4).

Case I The first case corresponds to $B+\delta < 0$ and a more physically realistic parameter regime where grass is more effective at attenuating erosion. In this parameter regime, δ is smaller and therefore, the erosion rate decays faster as a function of grass. From (3.8), it is clear that $\tilde{G}_- < 0 < \tilde{G}_+$ and there exists only one peak for positive values of G, given by the value of $\tilde{G}_+$. Further, since $K(0) = 1$, this means that for $e_1 < 1$, there exists only one positive steady state and for $e_1 > 1$, there exist two positive steady states (Fig. 4a). The two positive steady states collide and annihilate each other at the saddle-node bifurcation point e_1^*, given by:

$$e_1^* = K(\tilde{G}_+) = \frac{2e_3 A(\delta^2 + B\delta - Ae_3) + (2Ae_3 - B\delta)\sqrt{A^2 e_3^2 - Ae_3\delta(B+\delta)}}{\delta^2 \sqrt{A^2 e_3^2 - Ae_3\delta(B+\delta)}}.$$

Case II Case II corresponds to $B+\delta \geq 0$, a parameter regime in which cordgrass is less effective at attenuating sediment erosion. From (3.8), it is clear that $\tilde{G}_- < \tilde{G}_+ < 0$ and there exist no peaks for positive values of G. Therefore, since $K(0) = 1$, for

$e_1 < 1$, we have one positive steady state, while for $e_1 > 1$ there is no positive steady state (Fig. 4b). $\qquad\qquad\qquad\qquad\qquad\qquad\qquad\qquad\qquad\qquad\qquad\qquad\qquad\square$

Now that we know how many positive steady states can be expected, we evaluate their stability and obtain the following theorem:

Theorem 3.3 *Suppose that $p_1, e_1, e_3, \phi > 0$, $0 < \delta < 1$ and let A and B be defined as in (3.2). For the positive steady states $E_{GS} = (G^*_\pm, S^*_\pm)$ defined as:*

$$
\begin{aligned}
G^*_\pm &= \frac{-(e_1\delta + B) \pm \sqrt{(e_1\delta + B)^2 - 4Ae_3(e_1 - 1)}}{2A}, \\
S^*_\pm &= \frac{G^*_\pm + e_3}{\delta G^*_\pm + e_3},
\end{aligned}
\tag{3.9}
$$

we have the following cases:

1. (***Case I***) *Let $B + \delta < 0$. For $1 < e_1 < e_1^*$ where e_1^* is defined as in (3.3), the high density positive steady state $(G^{*+}, \frac{1}{L(G^*_+)})$ is locally asymptotically stable and the low density positive steady state $(G^*_-, \frac{1}{L(G^*_-)})$ is unstable. For $0 < e_1 \le 1$, there is only one positive steady state $(G^{*+}, \frac{1}{L(G^*_+)})$ which is locally asymptotically stable.*
2. (***Case II***) *Let $B + \delta \ge 0$. Then, for all $0 < e_1 < 1$, the unique positive steady state $(G^*_+, \frac{1}{L(G^*_+)})$ is locally asymptotically stable.*

Proof We first evaluate the Jacobian matrix **J** of system (3.1) at the positive steady state E_{GS}. This is given by:

$$
\mathbf{J}(E_{GS}) = \begin{bmatrix} -G^* & G^*F'(\frac{1}{L(G^*)}) \\ -\phi\frac{1}{L(G^*)}L'(G^*) & -\phi L(G^*) \end{bmatrix}.
$$

This is just the general form of the Jacobian evaluated at the positive steady state type. From Theorem 3.2, we can have either two such positive states (high and low) or just one, depending on the parameter regime. We will consider both cases in this proof. We note the special form of the Jacobian matrix, reflecting the cooperative nature of our system:

$$
\mathbf{J} = \begin{bmatrix} - & + \\ + & - \end{bmatrix}.
$$

From **J**, we can define the trace and determinant as follows:

$$
\begin{aligned}
\operatorname{Tr}\mathbf{J} &= -G^* - \phi L(G^*), \\
\operatorname{Det}\mathbf{J} &= \phi G^* L(G^*) + \phi \frac{1}{L(G^*)} G^* L'(G^*) F'\left(\frac{1}{L(G^*)}\right).
\end{aligned}
$$

In order for E_{GS} to be locally asymptotically stable, we need $\mathrm{Tr}\,\mathbf{J} < 0$ and $\mathrm{Det}\,\mathbf{J} > 0$. Since $L(G^*) \geq 0$ and G^* is a positive quantity, the trace of $\mathbf{J}$ is always negative. Note that since $\mathrm{Tr}\,\mathbf{J} < 0$, a Hopf bifurcation cannot occur from the positive steady state. Therefore, to assess stability, we need to determine the sign of $\mathrm{Det}\,\mathbf{J}$. Using (3.4) and (3.6), we can rewrite $\mathrm{Det}\,\mathbf{J}$ in terms of $K'(G)$ to obtain:

$$
\begin{aligned}
\mathrm{Det}\,\mathbf{J} &= \phi G^*\left(L(G^*) + \frac{1}{L(G^*)}L'(G^*)F'\left(\frac{1}{L(G^*)}\right)\right) \\
&= \phi G^*\left(L(G^*) + \frac{1}{L(G^*)}L'(G^*)\frac{p_1 + e_1}{\left(\frac{1}{L(G^*)} + p_1\right)^2}\right) \\
&= \phi G^*\left(L(G^*) + \frac{1}{L(G^*)}L'(G^*)\frac{p_1 + \frac{1-G^*}{L(G^*)} - p_1 G^*}{\left(\frac{1}{L(G^*)} + p_1\right)^2}\right) \\
&= \phi G^*\left(L(G^*) + \frac{L'(G^*)(1 - G^*)}{1 + L(G^*)p_1}\right) \\
&= \phi G^*\left(\frac{-K'(G^*)L^2(G^*)}{1 + L(G^*)p_1}\right).
\end{aligned}
$$

From Eq. (3.4), we can solve the steady states explicitly as in (3.9). We now consider two cases from Theorem 3.2. For Case I, both low and high steady states (G_+^*, S_+^*) and (G_-^*, S_-^*) are positive, while for Case II, only the high positive steady state (G_+^*, S_+^*) is positive. These are the steady states we consider and assess their stability.

Case I For Case I $(B + \delta < 0)$, we have the following scenarios:

- **(i)** For $1 < e_1 < e_1^*$, there are two positive steady states (G_+^*, S_+^*) and (G_-^*, S_-^*). From the definitions of the steady states in (3.9), it follows that

$$
\begin{aligned}
-e_1\delta - B &> \sqrt{(e_1\delta + B)^2 - 4Ae_3(e_1 - 1)} > 0, \\
(e_1\delta + B)^2 &> 4A(e_1 e_3 - e_3).
\end{aligned}
\tag{3.10}
$$

Evaluating $K'(G)$ from Eq. (3.6) at $G = G_+^*$ and $G = G_-^*$ yields:

$$
\begin{aligned}
K'(G_+^*) &= \frac{-2\delta(-e_1\delta - B)^2 - 2\delta(-e_1\delta - B)C + 8\delta Ae_3(e_1 - 1) - 4Ae_3C}{4A(\delta G_+^* + e_3)^2}, \\
K'(G_-^*) &= \frac{-2\delta(-e_1\delta - B)^2 + 2\delta(-e_1\delta - B)C + 8\delta Ae_3(e_1 - 1) + 4Ae_3C}{4A(\delta G_-^* + e_3)^2},
\end{aligned}
\tag{3.11}
$$

with

$$
C = \sqrt{(e_1\delta + B)^2 - 4Ae_3(e_1 - 1)} > 0.
$$

Using conditions from (3.10), we can show:

$$
\begin{aligned}
K'(G_+^*) &= \frac{-2\delta(-e_1\delta - B)^2 - 2\delta(-e_1\delta - B)C + 8\delta Ae_3(e_1 - 1) - 4Ae_3C}{4A(\delta G_+^* + e_3)^2} \\
&< \frac{-2\delta(-e_1\delta - B)^2 - 2\delta(-e_1\delta - B)C + 2\delta(e_1\delta + B)^2 - 4Ae_3C}{4A(\delta G_+^* + e_3)^2} \\
&= \frac{-2\delta(-e_1\delta - B)C - 4Ae_3C}{4A(\delta G_+^* + e_3)^2} < 0,
\end{aligned}
\tag{3.12}
$$

and

$$
\begin{aligned}
K'(G_-^*) &= \frac{-2\delta(-e_1\delta - B)^2 + 2\delta(-e_1\delta - B)C + 8\delta Ae_3(e_1 - 1) + 4Ae_3C}{4A(\delta G_-^* + e_3)^2} \\
&> \frac{-2\delta(-e_1\delta - B)^2 + 2\delta C^2 + 8\delta Ae_3(e_1 - 1) + 4Ae_3C}{4A(\delta G_-^* + e_3)^2} \\
&= \frac{4Ae_3C}{4A(\delta G_-^* + e_3)^2} > 0.
\end{aligned}
\tag{3.13}
$$

Therefore, since $K'(G) < 0$ on the (G_+^*, S_+^*) branch, Det $\mathbf{J}$ evaluated at (G_+^*, S_+^*) is positive and (G_+^*, S_+^*) is locally asymptotically stable. Similarly, since $K'(G) > 0$ on the (G_-^*, S_-^*) branch, Det $\mathbf{J}$ evaluated at (G_-^*, S_-^*) is negative and (G_-^*, S_-^*) is unstable.

- **(ii)** For $0 < e_1 \leq 1$, there is only one positive steady state branch corresponding to $(G_+^*, \frac{1}{L(G_+^*)})$. Further, we can show that

$$
0 < -\delta - B < -e_1\delta - B.
$$

From (3.11), it then follows that $K'(G_+^*) < 0$. Since Det $\mathbf{J}$ evaluated at (G_+^*, S_+^*) is positive, (G_+^*, S_+^*) is locally asymptotically stable.

Case II For Case II ($B + \delta \geq 0$), there is a unique positive steady state branch corresponding to (G_+^*, S_+^*). From Eq. (3.6) it is clear that $K'(G) < 0$ for all positive values of G. Therefore, since Det $\mathbf{J}$ evaluated at (G_+^*, S_+^*) is positive, the steady state (G_+^*, S_+^*) is locally asymptotically stable.   □

The results from Proposition 3.1, Theorems 3.2 and 3.3 are summarized in Fig. 5. In Case I, the system displays bistability for values $1 < e_1 < e_1^*$, where both the high positive steady state and the trivial steady state are stable, separated by an unstable positive steady state branch. The two positive steady states then merge in a saddle-node bifurcation at e_1^*, after which only the stable trivial steady state E_S remains. Bistability is not surprising given the highly cooperative nature of this system and large role that the grass plays in erosion mitigation. In Case II, which corresponds to the scenario where grass is less effective at attenuating erosion, the unique stable positive state gradually decreases and eventually undergoes a transcritical bifurcation at $e_1 = 1$ at which it exchanges stability with the trivial steady state E_S. Note that the positive
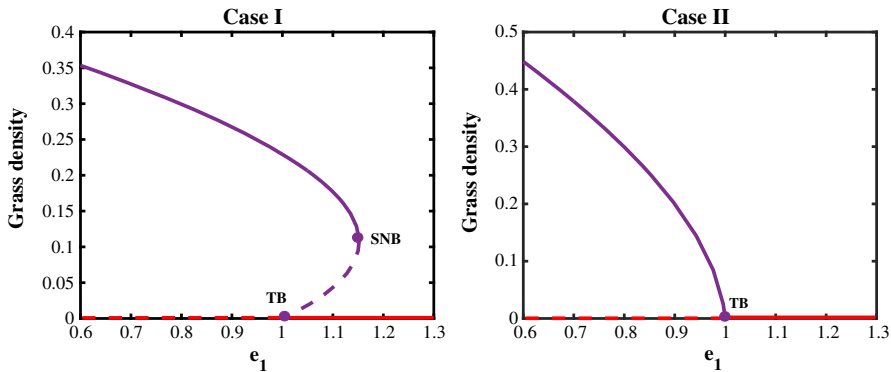
Fig. 5 Bifurcation diagrams plotted using MatCont (Dhooge et al. 2008) for Case I with a saddle-node (SNB) bifurcation happening at $e_1 = 1.16$ and a transcritical (TB) bifurcation happening at $e_1 = 1$ and Case II with only a transcritical bifurcation happening at $e_1 = 1$. Parameters used in Case I: $p_1 = 3.5, \phi = 0.14, e_3 = 0.1140, \delta = 1/7$. Parameters used in Case II: $p_1 = 0.5, \phi = 0.14, e_3 = 0.5, \delta = 0.3$ (color figure online)

steady state in Case II ceases to exist for smaller values of $e1$ than in Case I. This is intuitive as Case I corresponds to a more cooperative parameter regime that makes population persistence more possible.

3.2 Generalized cooperative system with nonlocal interactions

We now consider the spatially extended system to investigate the emergence of a patterned solution. Given the complexity of the spatially extended system (2.4), we carry out a steady state biharmonic approximation of this system, allowing us to perform linear stability analysis on the approximated system and gain insight into the dynamics of the original system (2.4) (Murray 2001; D'Odorico et al. 2006; Borgogno et al. 2009).

Let's consider the following general form of our system (2.4):

$$\begin{cases} \partial_t u = d_{11}\partial_x^2 u + f(u,v), & x \in \mathbb{R}, t > 0, \\ \partial_t v = d_{22}\partial_x^2 v + g(u,v) + \lambda v \int_{-\infty}^{\infty} P(x-x')u(x')dx', & x \in \mathbb{R}, t > 0, \ (3.14) \\ u(x,0) = u_0(x) \geq 0, \quad v(x,0) = v_0(x) \geq 0, & x \in \mathbb{R}. \end{cases}$$

where $P(x)$ is defined the same as in (2.2), and f, g are general smooth functions. Following standard procedure, we assume the kernel has a limited effect at relatively large distances and perform a Taylor's expansion of the integral term around $x' = x$ (Murray 2001, pp. 482–489):

$$\int_{-\infty}^{\infty} P(x-x')u(x')dx' = \int_{-\infty}^{\infty} P(z)u(x-z)dz$$

$$= \int_{-\infty}^{\infty} P(z)\left[u(x) - z\frac{\partial u(x)}{\partial x} + \frac{z^2}{2!}\frac{\partial^2 u(x)}{\partial x^2} - \frac{z^3}{3!}\frac{\partial^3 u(x)}{\partial x^3} + \frac{z^4}{4!}\frac{\partial^4 u(x)}{\partial x^4} - \cdots\right]dz.$$

This is a reasonable assumption in the context of our model as the scale-dependent grass–sediment feedback is thought to occur on a relatively small spatial scale (1–4 m). We can then define the moments P_m in the following way:

$$P_m = \frac{1}{m!} \int_{-\infty}^{\infty} z^m P(z)dz, \quad m = 0, 1, 2, \ldots$$

Given the symmetry of the kernel $P(x)$, the odd-power moments vanish, as does P_0 since $\int_{-\infty}^{\infty} P(x')dx' = 0$. From the specific form of the Mexican-hat kernel in (2.2), we can obtain exact expressions for P_2 and P_4 in term of the variances σ_1 and σ_2 of the excitatory and inhibitory effects, respectively:

$$P_2 = \frac{\sigma_1^2 - \sigma_2^2}{2} < 0, \quad P_4 = \frac{\sigma_1^4 - \sigma_2^4}{8} < 0. \tag{3.15}$$

To account for both short-range and long-range cross-diffusion, we truncate the expansion at the fourth partial derivative. The original system (3.14) can now be approximated by the following biharmonic system (Bates and Ren 1996, 1997; Couteron and Lejeune 2001):

$$\begin{cases} \partial_t u = d_{11}\partial_x^2 u + f(u, v), & x \in \mathbb{R}, t > 0, \\ \partial_t v = d_{22}\partial_x^2 v + g(u, v) + \lambda v(P_2\partial_x^2 u + P_4\partial_x^4 u), & x \in \mathbb{R}, t > 0, \\ u(x, 0) = u_0(x, 0) \geq 0, \quad v(x, 0) = v_0(x, 0) \geq 0, & x \in \mathbb{R}. \end{cases} \tag{3.16}$$

In this way, the evolution of u and v now depends not only on their own diffusion as in the classic reaction–diffusion system, but also on the additional short-range cross-diffusion $\partial_x^2 u$ and long-range cross-diffusion $\partial_x^4 u$ terms. Here, $\lambda v P_2$ and $\lambda v P_4$ represent the corresponding cross-diffusion coefficients. We are interested in the conditions that lead to the emergence of a spatially patterned solution in such a system. In general, spatial patterns arise in such systems through Turing instability, a symmetry breaking mechanism in which an otherwise stable spatially uniform steady state is destabilized by the addition of diffusion and cross-diffusion terms. To derive conditions for such an instability, we perform a classic Turing type linear stability analysis on the approximated system (3.16).

We expand our system (3.16) about a spatially uniform positive steady state (u^*, v^*) with $u^* > 0$ and $v^* > 0$. Substituting

$$u(x, t) = u^* + w_1(x, t), \quad |w_1(x, t)| \ll u^*,$$
$$v(x, t) = v^* + w_2(x, t), \quad |w_2(x, t)| \ll v^*,$$

into (3.16) and dropping any nonlinear terms, the resulting linearized system about (u^*, v^*) becomes:

$$\mathbf{W_t} = \mathbf{JW} + \mathbf{D}\nabla^2\mathbf{W} + \mathbf{H}\nabla^4\mathbf{W}, \tag{3.17}$$

with

$$\mathbf{W}(x, t) = \begin{pmatrix} w_1(x, t) \\ w_2(x, t) \end{pmatrix}, \quad \mathbf{D} = \begin{pmatrix} d_{11} & 0 \\ d_{21} & d_{22} \end{pmatrix},$$

$$\mathbf{H} = \begin{pmatrix} 0 & 0 \\ h_1 & 0 \end{pmatrix}, \quad \mathbf{J} = \begin{pmatrix} f_u & f_v \\ g_u & g_v \end{pmatrix}\Big|_{(u^*, v^*)}, \tag{3.18}$$

where

$$d_{21} = \lambda v^* P_2 < 0, \quad h_1 = \lambda v^* P_4 < 0; \quad d_{11}, d_{22} > 0. \tag{3.19}$$

Here, we consider a cooperative form of $\mathbf{J}$ with $f_u, g_v < 0$ and $f_v, g_u > 0$:

$$\mathbf{J} = \begin{pmatrix} - & + \\ + & - \end{pmatrix}, \tag{3.20}$$

Note that this is different from the classic Turing model activator–inhibitor form of $\mathbf{J}$ where f_u and g_v are of opposite sign.

Following standard convention, we let

$$\mathbf{W}(x, t) = \begin{pmatrix} w_1(x, t) \\ w_2(x, t) \end{pmatrix} = \begin{pmatrix} a \\ b \end{pmatrix} e^{\alpha t + ikx}. \tag{3.21}$$

Here, a and b are constants, and k is the corresponding wavenumber, with $1/k$ being proportional to the wavelength of the emergent patterns. Since e^{ikx} is periodic and bounded, the sign of α plays an important role in determining whether these small perturbations away from the steady state will grow or decay.

Substituting (3.21) into (3.17) and looking for a nontrivial solution, we require

$$|\alpha \mathbf{I} - \mathbf{J} + k^2 \mathbf{D} - k^4 \mathbf{H}| = \begin{vmatrix} \alpha + d_{11}k^2 - f_u & -f_v \\ -g_u + k^2 d_{21} - k^4 h_1 & \alpha + d_{22}k^2 - g_v \end{vmatrix} = 0. \tag{3.22}$$

This yields the following dispersion relation:

$$\alpha^2 - b(k^2)\alpha + c(k^2) = 0, \tag{3.23}$$

where

$$b(k^2) = \mathrm{Tr}\,\mathbf{J} - k^2 \,\mathrm{Tr}\,\mathbf{D},$$
$$c(k^2) = (\mathrm{Det}\,\mathbf{D} - f_v h_1)k^4 - (d_{11}g_v + d_{22}f_u - f_v d_{21})k^2 + \mathrm{Det}\,\mathbf{J}. \tag{3.24}$$

Using this dispersion relation, we can then derive conditions for Turing type instability, summarized in the following theorem:

Theorem 3.4 *Let* (u^*, v^*) *be a constant steady state solution of* (3.16) *with* **D** *defined as in* (3.18) *with* $d_{11}, d_{22} > 0$ *and* $P_2 < 0$ *and* $P_4 < 0$ *defined in* (3.15)*. Also, let* **J** *be defined as in* (3.20) *with* $f_u, g_v < 0$ *and* $f_v, g_u > 0$*. If*

$$\text{Det } \mathbf{J} > 0,$$
$$d_{11}g_v + d_{22}f_u - f_v\lambda v^* P_2 > 2\sqrt{\text{Det}(\mathbf{D}) - f_v\lambda v^* P_4}\sqrt{\text{Det}(\mathbf{J})} > 0, \tag{3.25}$$

then (u^*, v^*) *is locally asymptotically stable with respect to the corresponding ODE system, but is unstable with respect to system* (3.16)*.*

Proof The solution to (3.23) yields:

$$\alpha_\pm(k^2) = \frac{b(k^2) \pm \sqrt{[b(k^2)]^2 - 4c(k^2)}}{2}. \tag{3.26}$$

Note that $k^2 = 0$ corresponds to the spatially homogeneous case. For Turing instability, we require the spatially homogeneous state (u^*, v^*) to be stable in the absence of spatial variation $(k^2 = 0)$. Therefore, for $k^2 = 0$, the eigenvalues given in (3.26) have to be negative. This occurs when the trace of **J** is negative and the determinant of **J** is positive. From the special form of our matrix **J** in (3.20), it is clear that the trace of **J** is always negative, and from the first assumption in (3.25) know that the determinant of **J** is positive. So (u^*, v^*) is locally asymptotically stable with respect to the corresponding ODE system.

For the emergence of a non-constant spatially periodic solution, we further require that for some $k^2 \neq 0$, $\text{Re}(\alpha_+(k^2)) > 0$, guaranteeing that the perturbation will grow. Since $\text{Tr } \mathbf{D} > 0$ and $\text{Tr } \mathbf{J} < 0$, a necessary but not sufficient condition is that

$$c(k^2) < 0 \quad \text{for some } k^2 \in \mathbb{R}_+.$$

This happens as long as the following condition is satisfied:
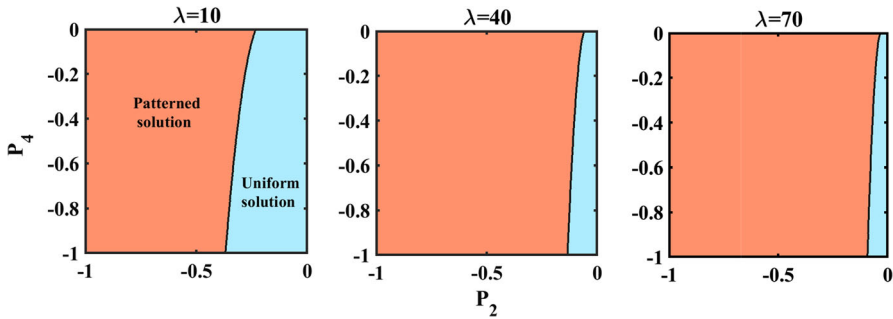
$$d_{11}g_v + d_{22}f_u - f_vd_{21} > 0. \tag{3.27}$$

Under the condition (3.27), the minimum of $c(k^2)$ is achieved at some $k^2 = k_m^2 > 0$. Minimizing $c(k^2)$ with respect to k^2 yields:

$$c_{min} = \min_{k^2} c(k^2) = c(k_m) = \text{Det}(\mathbf{J}) - \frac{(d_{11}g_v + d_{22}f_u - f_vd_{21})^2}{4(\text{Det}(\mathbf{D}) - f_vh_1)},$$
$$k_m^2 = \frac{d_{11}g_v + d_{22}f_u - f_vd_{21}}{2(\text{Det}(\mathbf{D}) - f_vh_1)}. \tag{3.28}$$

Guaranteeing that $c_{min} < 0$, we then have the following final condition:

$$d_{11}g_v + d_{22}f_u - f_vd_{21} > 2\sqrt{\text{Det } \mathbf{D} - f_vh_1}\sqrt{\text{Det } \mathbf{J}}. \tag{3.29}$$

□

Fig. 6 Parameter space of Turing-like instability satisfying conditions (3.34) for various values of P_2 and P_4 with fixed λ. Note that increasing the value of λ, results in a larger parameter space. It is also clear that patterns are possible even in the absence of the fourth order term ($P_4 = 0$). The following parameters are used: $N = 0.06$, $M = -0.13$, $\det \mathbf{J} = 0.004$, $\det \mathbf{D} = 0.024$ derived from the original model with $e_1 = 1.05$, $p_1 = 3.5$, $\phi = 0.14$, $e_3 = 0.1140$, $\delta = 1/7$, $D_G = 0.04$, $D_S = 0.6$ (color figure online)

Now, the same range of wavenumbers k that makes $c(k^2) < 0$ in (3.24) also guarantees that $\mathrm{Re}(\alpha(k^2)) > 0$. We can further calculate the relevant range of wavenumbers $k_-^2 < k^2 < k_+^2$ by computing the zeros of the function $c(k^2)$ such that $c(k_-^2) = c(k_+^2) = 0$. Then

$$
\begin{aligned}
k_-^2 &= \frac{B(J, D) - \sqrt{B(J, D)^2 - 4 \operatorname{Det} J (\operatorname{Det} D - f_v h_1)}}{2(\operatorname{Det} D - f_v h_1)} < k^2 \\
&< \frac{B(J, D) + \sqrt{B(J, D)^2 - 4 \operatorname{Det} J (\operatorname{Det} D - f_v h_1)}}{2(\operatorname{Det} D - f_v h_1)} = k_+^2,
\end{aligned}
\tag{3.30}
$$

where

$$
B(J, D) = d_{11} g_v + d_{22} f_u - f_v \lambda v^* P_2
\tag{3.31}
$$

The spatial patterns that emerge have a corresponding wavelength ω, defined as

$$
\omega = \frac{2\pi}{k_m},
$$

with k_m defined in (3.28) in the interval (3.30) and the one for which the positive eigenvalue $\alpha_+(k^2)$ from (3.26) achieves a maximum, corresponding to the most unstable and fastest growing mode.

We can gain further insight into the result from Theorem 3.4 by visualizing the instability conditions in the $P_2 P_4$-plane (Fig. 6). Letting

$$
M = d_{11} g_v + d_{22} f_u, \quad N = f_v v^*,
\tag{3.32}
$$

the second stability condition from Theorem 3.4 is equivalent to

$$
(M - \lambda N P_2)^2 - 4 \operatorname{Det}(\mathbf{J})(\operatorname{Det}(\mathbf{D}) - \lambda N P_4) > 0.
\tag{3.33}
$$

Further rearrangement of (3.33) leads to the following condition for the instability of the uniform solution:

$$P_4 > \frac{-P_2^2 N^2 \lambda^2 + 2 P_2 M N \lambda - (M^2 - 4 \operatorname{Det}(\mathbf{J}) \operatorname{Det}(\mathbf{D}))}{4 N \operatorname{Det}(\mathbf{J}) \lambda}. \qquad (3.34)$$

Additionally, we have

$$M^2 - 4 \operatorname{Det}(\mathbf{D}) \operatorname{Det}(\mathbf{J}) = (d_{11} g_v - d_{22} f_u)^2 + 4 d_{11} d_{22} f_v g_u > 0. \qquad (3.35)$$

Note that the first stability condition from (3.25) in Theorem 3.4 is independent of P_2, P_4 and λ. Therefore, given that this first condition holds, rearranging the other instability condition in Theorem 3.4 in the form of (3.34) and using (3.35) as well as the fact that $M < 0$ and $N > 0$, it is clear that the instability region corresponds to the area to the left of the downward facing parabola defined on the right hand side of (3.34) in the fourth quadrant of the $P_2 P_4$-plane (Fig. 6). Without the activator–inhibitor dynamics, a cooperative system cannot be destabilized by diffusion alone. Theorem 3.4 makes it clear that the additional cross-diffusion terms given by P_2 and P_4 make spatial heterogeneous patterns possible in this cooperative system. In particular, the cross-diffusion term with P_2 plays a crucial role in the pattern forming mechanism since in its absence ($P_2 = 0$), the term $c(k^2)$ from the dispersion relation in (3.23) can never be negative for any k^2. Since the biharmonic parameter P_4 acts as a stabilizing force, we also note that as its absolute value increases, the window for spatial patterns decreases (Fig. 6). Increasing the value of the strength parameter λ offsets the effect of the biharmonic parameter P_4 and increases the size of the window in which spatial patterns are possible. We note that in the absence of the biharmonic long-range cross-diffusion term ($P_4 = 0$), the conditions for Turing instability can still be satisfied. In this case, the system is reduced to a special case of the reaction–diffusion model with cross-diffusion, for which Turing instability conditions have been previously derived (Madzvamuse et al. 2015).

Previous results in this section took into consideration the system on an infinite domain $\mathbb{R}$. In such a system, we will always find an unstable mode k^2 in the interval (3.30) if the conditions in Theorem 3.4 are satisfied. Numerical simulations require the choice of a finite domain with specific boundary conditions. Therefore, we now consider the scenario on a bounded domain $T = (-l, l)$ with periodic boundary conditions, where the size of T also affects the pattern formation. This is a more restrictive situation than the infinite domain scenario as the wavenumbers k are now discrete and depend on the size of the domain. In this case, we shall understand that the solution (u, v) on T are periodically extended to $\mathbb{R}$ so the integral terms in the original system is still integrated on $\mathbb{R}$.

The result for the bounded domain case is summarized in the following corollary:

Corollary 3.5 *Consider* (3.16) *on a finite domain* $T = \{x \in \mathbb{R} : -l < x < l\}$ *and the following periodic boundary conditions:*

$$\begin{aligned} u(-l, t) &= u(l, t), \quad u_x(-l, t) = u_x(l, t), \\ v(-l, t) &= v(l, t), \quad v_x(-l, t) = v_x(l, t). \end{aligned} \qquad (3.36)$$

Let (u^*, v^*) be a constant steady state solution of (3.16) with $\mathbf{D}$ defined as in (3.18) with $d_{11}, d_{22} > 0$ and $P_2 < 0$ and $P_4 < 0$ defined in (3.15). Also, let $\mathbf{J}$ be defined as in (3.20) with $f_u, g_v < 0$ and $f_v, g_u > 0$. If

$$\text{Det } \mathbf{J} > 0,$$

$$d_{11}g_v + d_{22}f_u - f_v\lambda v^* P_2 - 2\sqrt{\text{Det } \mathbf{J}(\text{Det } \mathbf{D} - f_v\lambda v^* P_4)} \qquad (3.37)$$

$$> \left(\frac{\pi}{l}\right)^2 (\text{Det } \mathbf{D} - f_v\lambda v^* P_4),$$

then (u^*, v^*) is locally asymptotically stable with respect to the corresponding ODE system, but is unstable with respect to system (3.16) on T with boundary condition (3.36). Moreover the most unstable mode is given by $n \in \mathbb{N}$ such that

$$\alpha(k_m^2) = \alpha_+ \left(\frac{n^2\pi^2}{l^2}\right) = \max_{i \in \mathbb{N}} \alpha_+ \left(\frac{i^2\pi^2}{l^2}\right), \qquad (3.38)$$

where $\alpha_+(k^2)$ is defined in (3.26), and the corresponding wavelength is $\omega = 2\pi/k_m = 2l/n$.

Proof The non-constant eigenfunctions that satisfy the corresponding eigenvalue problem $\phi'' + \lambda\phi = 0$ on the domain $(-l, l)$ with periodic boundary conditions are of the following form

$$\phi_i(x) = a_1 \sin\left(\frac{i\pi x}{l}\right) + a_2 \cos\left(\frac{i\pi x}{l}\right), \quad i \in \mathbb{N},$$

and the corresponding eigenvalues are $k_i = (i\pi/l)^2$ for $i \in \mathbb{N}$. Now, when $0 < k_-^2 < k_i^2 = (i\pi/l)^2 < k_+^2$ for some $i \in \mathbb{N}$, where k_- and k_+ are defined in (3.30), the eigenvalue $\alpha_+(k_i^2)$ defined in (3.23) is positive for this i.

We then note that the discrete wavenumber k increases by π/l with each i. Therefore, to guarantee that we have at least one $k^2 = (i\pi/l)^2$ in the interval given by (k_-^2, k_+^2), it is sufficient that the length of the interval (k_-, k_+) is larger than π/l (Shi et al. 2011). Using

$$(k_+ - k_-)^2 = (k_-^2 + k_+^2) - 2k_1^+ k_2^- > \left(\frac{\pi}{l}\right)^2,$$

and the expressions of k_- and k_+ in (3.30), we obtain the second instability condition in (3.37). Now, for an interval of length $2l$, if the instability conditions (3.37) are satisfied, then a spatially patterned solution will emerge with the corresponding wavenumber $k = i\pi/l$ such that $k^2 \in (k_-^2, k_+^2)$. The most unstable wavenumber k_m is the one that maximizes $\alpha_+(k^2)$ in (3.26). ☐

The second instability condition in (3.37) also defines a minimal length l_m for the emergence of the spatial patterns:

$$l > l_m = \pi \sqrt{\frac{\text{Det } \mathbf{D} - f_v\lambda v^* P_4}{d_{11}g_v + d_{22}f_u - f_v\lambda v^* P_2 - 2\sqrt{\text{Det } \mathbf{J}(\text{Det } \mathbf{D} - f_v\lambda v^* P_4)}}}.$$

This implies that in numerical simulations, if one chooses $l < l_m$, then no spatial patterns can be observed. On the other hand, when the length l is large, then the interval (k_-, k_+) may contain multiple unstable wavenumbers $k = i\pi/l$, and the spatial patterns with all these wavenumebrs are possible but the one with most unstable wavenumber k_m is the one most likely to be observed.

3.3 Grass–sediment cooperative system with nonlocal interactions

We now apply these results to our Grass–Sediment system (2.4). The biharmonic approximation yields the following approximated system:

$$
\begin{cases}
\partial_t G = D_G \partial_x^2 G + G\big(F(S) - G\big), & x \in \mathbb{R}, t > 0 \\
\partial_t S = D_S \partial_x^2 S + \phi(-L(G)S + 1) + \lambda S(P_2 \partial_x^2 G + P_4 \partial_x^4 G), & x \in \mathbb{R}, t > 0 \\
G(x, 0) = G_0(x, 0) \geq 0, \quad S(x, 0) = S_0(x, 0) \geq 0, & x \in \mathbb{R},
\end{cases}
\tag{3.39}
$$

with $F(S)$, $L(G)$, P_2 and P_4 defined previously in Sects. 2 and 3.2. We note that the homogeneous steady state (G_+^*, S_+^*) for the corresponding ODE in Sect. 3.1 is still a solution of the corresponding spatially-explicit system (2.4) since $\int_{-\infty}^{\infty} P(x)dx = 0$. Therefore, following the biharmonic approximation, we can expand system (3.39) around the positive steady state (G_+^*, S_+^*) defined in (3.9) (Sect. 3.1), yielding:

$$
f_u = -G_+^*, \quad f_v = G_+^* F'\left(\frac{1}{L(G_+^*)}\right),
$$

$$
g_u = -\phi \frac{1}{L(G_+^*)} L'(G_+^*), \quad g_v = -\phi L(G_+^*).
$$

Note that the cooperative form of this system with $f_v, g_u > 0$ and $f_u, g_v < 0$. For numerical simulations, we consider this system on a finite domain $T = (-l, l)$ and the following periodic boundary conditions:
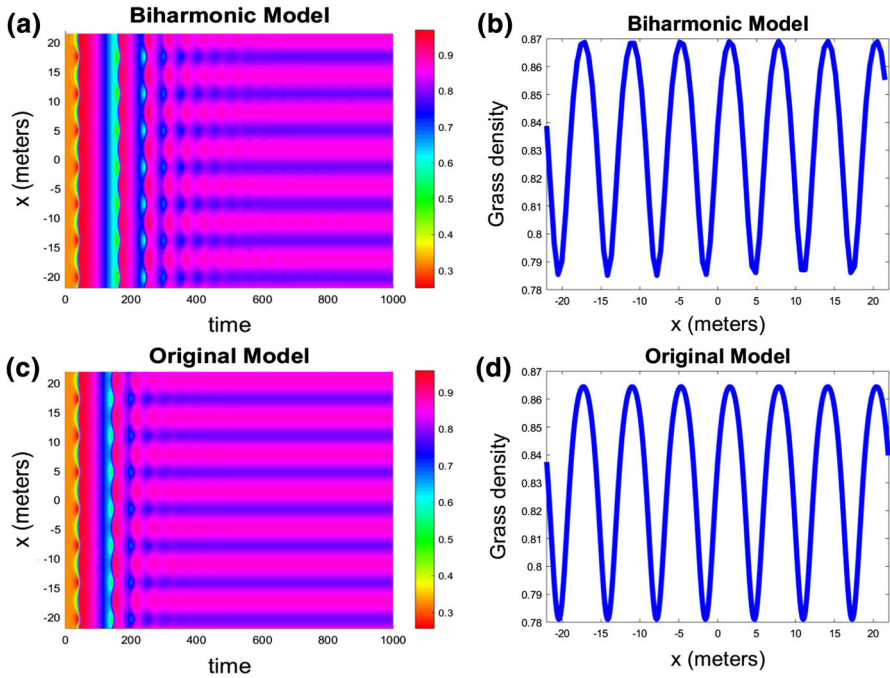
$$
G(-l, t) = G(l, t), \quad G_x(-l, t) = G_x(l, t),
$$
$$
S(-l, t) = S(l, t), \quad S_x(-l, t) = S_x(l, t).
$$

Using the results from Theorem 3.4 and Corollary 3.5, we have the following condition necessary for Turing instability on T:

$$
\begin{aligned}
D_G g_v + D_S f_u - f_v \lambda S^* P_2 - 2\sqrt{\text{Det}(\mathbf{D})} - f_v \lambda S^* P_4 \sqrt{\text{Det}(\mathbf{J})} \\
> \left(\frac{\pi}{l}\right)^2 (\text{Det } \mathbf{D} - f_v \lambda S^* P_4),
\end{aligned}
\tag{3.40}
$$

where

$$
\mathbf{D} = \begin{pmatrix} D_G & 0 \\ \lambda S^* P_2 & D_S \end{pmatrix}, \quad \mathbf{J} = \begin{pmatrix} f_u & f_v \\ g_u & g_v \end{pmatrix}\bigg|_{(G^*, S^*)}.
$$

(a)

(b)

(c)

(d)

Fig. 7 Spatial patterns produced through simulations of the biharmonic system (3.39) (**a**, **b**) and original system (3.16) (**c**, **d**) with Case I parameters: $D_G = 0.04$, $D_S = 0.6$, $\lambda = 40$, $e_1 = 0.7$, $p_1 = 3.5$, $f = 0.14$, $e_3 = 0.1140$, $\delta = \frac{1}{7}$ corresponding to the steady state values $G^* = 0.33$, $S^* = 2.75$. For the scale-dependent parameters, we use $\sigma_1 = 0.43$ and $\sigma_2 = .68$ in the original model and corresponding values of $P_2 = -0.1388$ and $P_4 = -0.0225$ for the biharmonic model. Both simulations are performed on a bounded domain $T = (-l, l) = (-7\pi, 7\pi)$. All parameters are chosen to satisfy conditions from (3.40). **a**, **c** Temporal evolution of the grass density while, **b**, **d** Final steady state of grass after 1000 time units. The characteristic wavelength is accurately predicted as $\omega = \frac{14\pi}{7}$ (color figure online)

For Case I parameter regime from Sect. 3.1, we choose: $e_1 = 0.7$, $p_1 = 3.5$, $f = 0.14$, $e_3 = 0.1140$, $\delta = 1/7$. We then choose $D_G = 0.04$, $D_S = 0.6$, $\lambda = 40$ for our nonlocal parameter values to satisfy the instability conditions (3.40) and numerically integrate the biharmonic system (3.39) on $T = (-l, l) = (-7\pi, 7\pi)$. We find that a spatially patterned solution emerges, as predicted (Fig. 7) and these simulations are also consistent with numerical simulations of the original system (2.4), suggesting that the theoretical results derived from the biharmonic system can be applied to the original system to give insight regarding under what conditions a spatially patterned solution emerges. The eigenvalue $\alpha_+(k^2)$ is given by:

$$\alpha_+(k^2) = -0.1893 - 0.32k^2$$
$$+ \frac{\sqrt{(-0.37858 - 0.64k^2)^2 - 0.44393k^4 + 1.35564k^2 - 0.03963}}{2}.$$

$$(3.41)$$
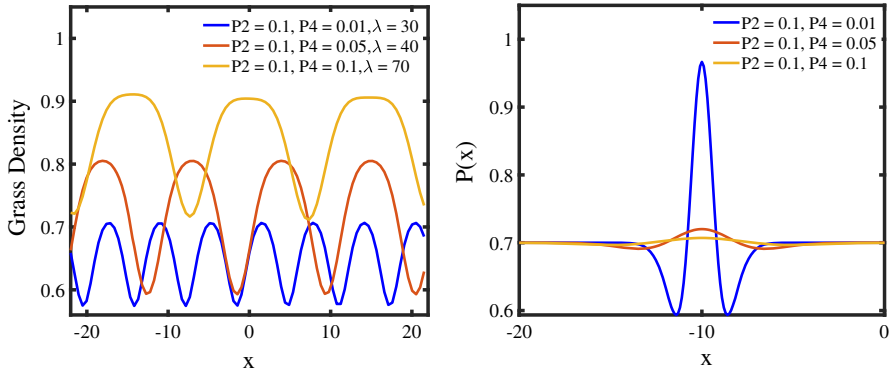
Fig. 8 a Displays the final steady states of grass after 1800 time units in the biharmonic system (3.39) for various values of P_2, P_4 and λ. Note that the value of λ has to be adjusted to offset increasing P_4 in order for patterns to emerge. Biologically realistic parameters are chosen such that conditions (3.40) are satisfied: $e_1 = 1.05$, $p_1 = 3.5$, $\phi = 0.14$, $e_3 = 0.1140$, $\delta = 1/7$, $D_G = 0.04$, $D_S = 0.6$. **b** Displays plots of kernel functions in (2.2) corresponding to parameters P_2 and P_4 from panel a) with larger values of parameter P_4 resulting in wider kernels (color figure online)

Furthermore, on the domain $T = (-7\pi, 7\pi)$, the range of wavenumbers for which the corresponding eigenvalue $\alpha_+(k^2)$ is positive is given by:

$$k_-^2 = 0.0295 < k^2 = \left(\frac{i\pi}{7\pi}\right)^2 < 3.0242 = k_+^2, \quad i \in \mathbb{N}. \qquad (3.42)$$

It can be calculated that for $2 \leq i \leq 12$, (3.42) is satisfied, and when $i = 7$, $\alpha_+(k^2)$ is maximized. Hence the characteristic wavelength of the emerging patterns is $\omega = 2l/7 = 2\pi$. This is consistent with simulation results which show 7 peaks (Fig. 7). Similar results are obtained for Case II parameter regime (see Fig. 11 in "Appendix" section.)

Previously, we used biologically realistic parameters from Table 1 (see "Appendix" section) to perform all numerical simulations, including realistic parameters for the scale-dependent feedback (P_2, P_4, λ). Now, we are interested in how varying these scale-dependent feedback parameters may affect the nature of the spatial patterns in system (3.39). As predicted in Sect. 3.2, since the biharmonic term P_4 acts as a stabilizing force, as its value gets larger, the window for spatial patterns decreases and a larger value of λ is necessary to offset its effect and allow spatial patterns to emerge (Fig. 8a). In addition, choosing a larger value of P_4 results in an overall increase in the pattern wavelength (Fig. 8a). This result can also be interpreted in the context of how the coefficients P_2 and P_4 are related to the shape of the kernel in (2.2) in the original system (2.4) (Fig. 8b). The coefficient P_2 measures the difference of the variances σ_1 and σ_2 of the excitatory and inhibitory interactions, respectively. The coefficient P_4 is related to kurtosis and controls the weight of the kernel's tails while λ modulates the amplitude of the Mexican-hat kernel. Since for a fixed value of P_2, an increase in P_4 results in a wider, flatter kernel shape, the wider the range of the long-range effects given by P_4, the stronger these interactions need to be (given by λ) to have a significant
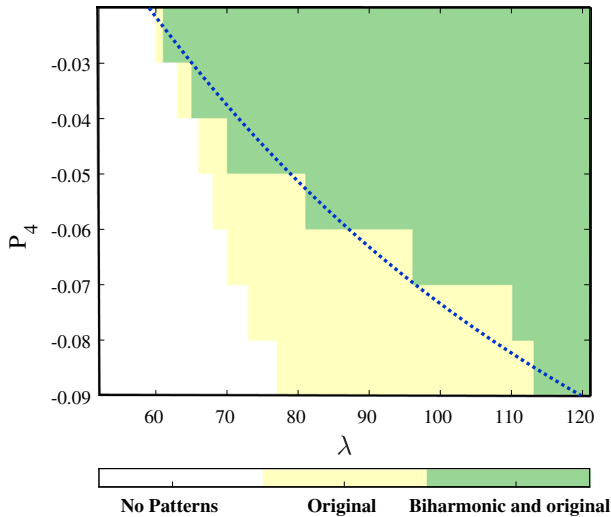
Fig. 9 We numerically integrate the fourth order biharmonic system (3.39) for different kernel widths (P_4) and kernel strengths (λ). Similarly, simulations of the original system (2.4) are performed for the corresponding kernel parameters σ_1 and σ_2 calculated from (3.15). All simulations are run over the same domain $T = (-7\pi, 7\pi)$ with the following parameters: $D_G = 0.04$, $D_S = 0.6$, $e_1 = 1.05$, $p_1 = 3.5$, $\phi = 0.14$, $e_3 = 0.1140$, $\delta = 1/7$, $P_2 = -0.05$. The region of instability derived from Corollary 3.5 corresponds to the area above the dotted blue curve. The results shown in green correspond to the instances where spatial patterns emerge for both the biharmonic system (3.39) and the original system (2.4), while the results in yellow correspond to instances where patterns emerged only for the original system (2.4). It is clear that the theoretical results from Corollary 3.5 (light blue curve) are consistent with the numerical simulations of the biharmonic system (region in green) and less consistent with the original system (region in yellow). Although these results are not as consistent, it is clear that the theoretical results can nonetheless be used to predict the formation of patterns in the original system (2.4) (color figure online)

effect and lead to the formation of spatial patterns. This makes biological sense, since the intensity of scale-dependent interactions tend to dissipate over larger distances and therefore need to be amplified to have any effect on spatial heterogeneity over longer ranges. In addition, we see that wider kernels result in wider spatial patterns characterized by longer wavelengths. Again, this makes biological sense as one would expect the scale of the spatial interactions to influence the resulting spatial patterns.

Finally, we compare our analytic results with numerical simulations of the approximated biharmonic system (3.39) and the original system (2.4) (Fig. 9). The analytic results from (3.40) are consistent with numerical simulations of the biharmonic system and the original system. However, we note that the onset of patterns in the original system occurs sooner than in the biharmonic system. Nonetheless, this result suggests that using the biharmonic system can help find the relevant parameter regime in which spatial patterns are possible in the original system and gain understanding into how the nature of the scale-dependent feedbacks affects the development of spatial patterns.

4 Discussion

We propose a phenomenological model to describe the dynamics of the marsh edge in terms of two-way interactions between marsh grass *Spartina alternifora* and sedimentation. In nature, the marsh edge can frequently be observed in a number of configurations ranging from a spatially uniform to a more wave-like shoreline. The interest of this paper lies in understanding whether the well-known scale-dependent (nonlocal) feedback between marsh vegetation and sedimentation can lead to spatially variable shoreline configurations. Marsh grass promotes sediment accretion in its immediate surroundings by slowing down current acts as a facilitation mechanism. In turn, the diverted water flow contributes to increased erosion further away and acts as an inhibitory mechanism. We propose a system of reaction–diffusion equations with an additional integral term with a Mexican-hat kernel function that describes the nature of this scale-dependent feedback. Our system is highly cooperative; as cooperative systems often lack the classic activator–inhibitor mechanism necessary for pattern formation, it becomes of interest how and under what conditions spatial patterns may develop.

We perform a biharmonic approximation of our system and carry out analysis on the simpler biharmonic system that expresses the kernel function as separate short-range and long-range diffusion terms. Using the more mathematically tractable biharmonic system, we are then able to derive general condition for the formation of spatial patterns in a cooperative system such as ours. Further, using numerical simulations, we confirm that the biharmonic model, while an approximation, is consistent with the original model, and therefore we can apply the theoretical results from the biharmonic system to help gain insight into the formation of patterns in the original system. We parameterize the kernel function using a set of reasonable parameters from literature and find that spatial patterns can develop, given that the scale-dependent interactions between marsh vegetation and sediment dynamics are strong enough. The model thus provides further evidence that the presence of scale-dependent interactions is essential for pattern formation and that heterogeneous patterns cannot occur in the presence of weak scale-dependent interactions. Not surprisingly, we find that the choice of wider kernels tend to produce wider spatial patterns (characterized by longer wavelengths) and vice versa. The nature and strength of the grass–sediment scale-dependent interactions depends on many factors such as the underlying hydrodynamics and sediment composition, the exact spatial scale (corresponding to the widths of the Mexican-hat kernel) and relative strength of the scale-dependent feedback are difficult to estimate in the field and can vary substantially. We use one possible set of biologically realistic parameters for the kernel function (Table 1) and find that the patterns that emerge in simulations occur on a spatial scale consistent with what can observed in nature (4–10 m between peaks) (Vandenbruwaene et al. 2011).

Furthermore, we find that there are two possible parameter regimes in the system. The first regime is especially of interest as it corresponds to a more realistic scenario where marsh vegetation is effective at attenuating erosion through the binding of sediment and decreasing the effect of wave erosion. Given the strong facilitatory nature of the grass–sediment interactions, bistability takes place in this parameter regime. In general, bistable dynamics makes a system especially prone to collapsing

to an irreversible state as environmental conditions gradually worsen and a tipping point is reached (Dakos et al. 2011; Kéfi et al. 2014, 2016) through the phenomenon of hysteresis. Pattern formation has previously been suggested as a possible coping mechanism for systems close to degradation (Chen et al. 2015). The analysis in this paper gives more insight into this previously reported phenomenon as we also find this to be the case in our model (Zaytseva et al. 2018) where pattern formation allows the marsh edge to cope with harsher erosion through spatial variation. One limitation of our model is the lack of multiple spatial dimensions as only the dynamics on a one-dimensional cross-section of the marsh edge were considered. Hence, we were not able to observe the geometry of the protrusions. In addition, the model is meant to be phenomenological in nature, omitting processes such as the effect and variation of hydrodynamics and wave action, modeled in more detail previously (Fagherazzi et al. 2012). As a future direction, we may consider a 2-dimensional extension of the model presented here in order to compare the 2-dimensional patterns produced by the model with those observed in the field. One challenge is the choice of an appropriate kernel for the 2-dimensional formulation as it is not immediately clear if the same kernel (but extended in 2 dimensions) would be appropriate or if the scale-dependent feedback has a preferential (lateral) direction across the marsh edge, in which case a one-dimensional kernel would be more fitting. Despite the relatively simple dynamics of our one-dimensional model, it is able to capture the pattern formation on the marsh edge as a result of scale-dependent feedbacks between vegetation and sediment accumulation. The agreement between the model simulations and field observations suggests that important pattern-generating processes have been captured in the model and non-local interactions between plants and sedimentation can drive the formation of shoreline patterns. In addition, the results in this paper can be generalized to any cooperative system with scale-dependent feedbacks in the form of short-range activation and long-range inhibition, described using a Mexican-hat kernel function.

5 Appendix

Figure 10 shows the plot of the functional forms of $F(S)$ and $L(G)$. Figure 11 shows numerical simulations of both the biharmonic system (3.39) and the original system (2.4) for the parameter regime in Case II from Sect. 3.1. We see that a spatially patterned solution emerges if the instability conditions in (3.40) are satisfied. Table 1 shows the biologically realistic parameters for the original system and their sources. We use the parameter values from Table 1 to obtain the new re-scaled parameters from Sect. 2 to use in all numerical simulations performed in this paper.

All numerical simulations in this paper are performed using MATLAB. We use an implicit finite differencing scheme to numerically integrate the original equation. Although this scheme is more computationally intensive, it is chosen because it is always numerically stable and convergent. Because domain size plays an important role in the system's ability to form patterns, a large enough domain has to be chosen
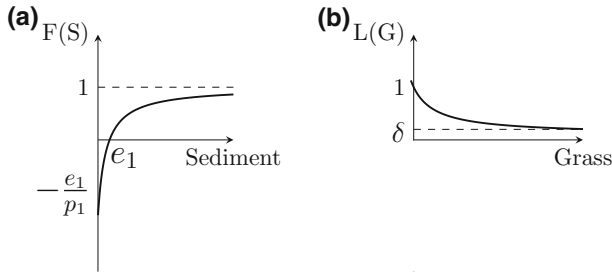
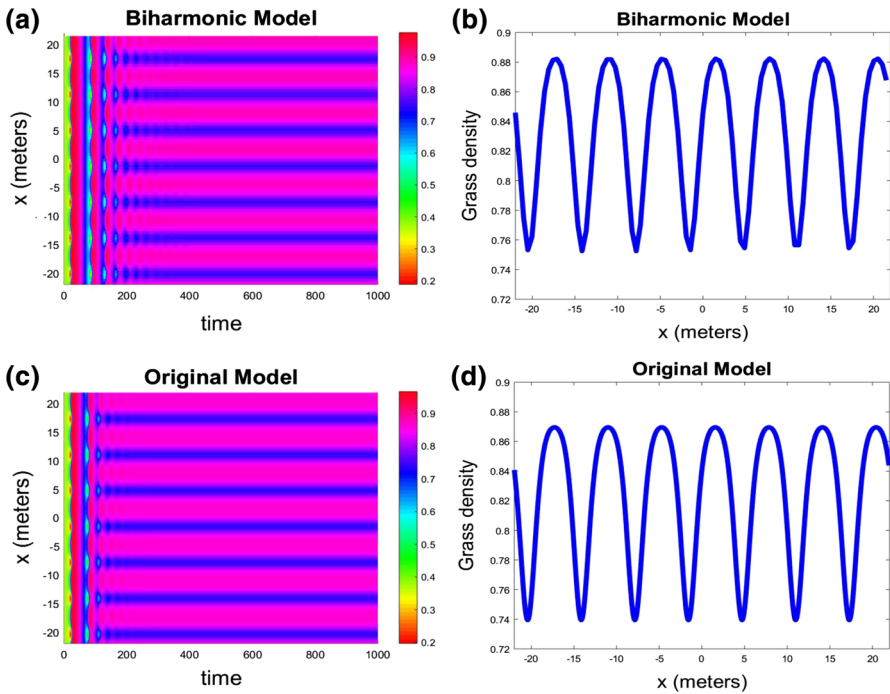**Fig. 10** Functions **a** $F(S)$, **b** $L(G)$ from (2.5)

Fig. 11 Spatial patterns produced through simulations of the biharmonic system (3.39) (**a, b**) and original system (3.16) (**c, d**) with Case II parameters: $D_G = 0.04$, $D_S = 0.6$, $\lambda = 40$, $e_1 = 0.7$, $p_1 = 0.5$, $f = 0.14$, $e_3 = 0.5$, $\delta = 0.3$. For the scale-dependent parameters, we use $\sigma_1 = 0.43$ and $\sigma_2 = 0.68$ in the original model and corresponding values of $P_2 = -0.1388$ and $P_4 = -0.0225$ for the biharmonic model. Both simulations are performed on a bounded domain $T = (-7\pi, 7\pi)$. All parameters are chosen to satisfy conditions from (3.40). **a, c** Temporal evolution of the grass density while, **b, d** final steady state of grass after 1000 time units. The characteristic wavelength is accurately predicted as $\omega = \frac{14\pi}{7}$ (color figure online)

to be able to fit patterns with their characteristic wavelength. We evaluate all integrals using the *trapz* function in MATLAB, which performs numerical integration using the trapezoidal rule. For the convolution term, we evaluate the integral of the product of the kernel and the periodically extended solution on the interval $(-3l, 3l)$, to make sure an adequate number of kernels are considered in calculating the net effect. To

Table 1 Biologically realistic parameters for the original system before non-dimensionalization

Symbol	Meaning	Unit	Value	Source
$\hat{D}_G$	Cordgrass diffusion coefficient	$m^2 \, year^{-1}$	0.06–0.135	Adams et al. (2012)
$\hat{D}_S$	Sediment diffusion coefficient	$m^2 \, year^{-1}$	0.876	Liu et al. (2014)
c	Self-limiting growth rate of cordgrass	$m^2 \, shoots^{-1} \, year^{-1}$	0.0057	Yang et al. (2014)
ψ	Minimum erosion rate	$year^{-1}$	0.002–0.3	Hardaway and Byrne (1999) and Rosen (1980)
k_s	Cordgrass density at which marsh erosion is half-maximal	shoots m^{-2}	30–50	Estimated
g	Erosion constant in the absence of cordgrass	Non-dimensional	5	Mariotti and Fagherazzi (2010) and Sheehan and Ellison (2015)
η	Sediment deposition rate	$m \, year^{-1}$	0.002–0.006	Stumpf (1983) and Goodman et al. (2007)
p^*	Intrinsic growth rate of cordgrass	$year^{-1}$	1.5	Yang et al. (2014)
l_1	Sediment threshold for cordgrass persistence	m	0.02	Estimated
l_1^*	Sediment elevation at which cordgrass growth is half-maximal	m	0.06	Estimated
$\hat{\lambda}$	Strength of nonlocal cordgrass–sediment interactions	$m^2 \, shoots^{-1} \, year^{-1}$	0.0004–0.3	Bouma et al. (2007)
σ_1	Standard deviation of the excitatory feedback for cordgrass	m	0.43	Bouma et al. (2007)
σ_2	Standard deviation of the inhibitory feedback for cordgrass	m	0.68	Bouma et al. (2007)

numerically integrate the biharmonic system, we use an explicit finite differencing scheme inMATLAB. This scheme is less computationally intensive, and is easier to implement, given the extra biharmonic term. For both models, the numerical simulations are performed on a spatial domain $(-l, l)$ with $l = 7\pi$ with periodic boundary conditions. We apply Turing's idea of diffusion driven instability and use a spatially periodic perturbation of the stable steady state of the corresponding system of ODEs as the initial condition for our simulations.

References

Adams J, Grobler A, Rowe C, Riddin T, Bornman T, Ayres D (2012) Plant traits and spread of the invasive salt marsh grass, *Spartina alterniflora* Loisel., in the Great Brak estuary, South Africa. Afr J Mar Sci 34(3):313–322

Altieri AH, Silliman BR, Bertness MD (2007) Hierarchical organization via a facilitation cascade in intertidal cordgrass bed communities. Am Nat 169(2):195–206

Amari S-I (1977) Dynamics of pattern formation in lateral-inhibition type neural fields. Biol Cybern 27(2):77–87

Balke T, Klaassen PC, Garbutt A, van der Wal D, Herman PMJ, Bouma TJ (2012) Conditional outcome of ecosystem engineering: a case study on tussocks of the salt marsh pioneer *Spartina anglica*. Geomorphology 153:232–238

Banerjee M, Volpert V (2016) Prey–predator model with a nonlocal consumption of prey. Chaos Interdiscip J Nonlinear Sci 26(8):083120

Barbier N, Couteron P, Lefever R, Deblauwe V, Lejeune O (2008) Spatial decoupling of facilitation and competition at the origin of gapped vegetation patterns. Ecology 89(6):1521–1531

Bates PW, Ren X (1996) Transition layer solutions of a higher order equation in an infinite tube. Commun Partial Differ Equ 21(1–2):109–145

Bates PW, Ren X (1997) Heteroclinic orbits for a higher order phase transition problem. Eur J Appl Math 8(02):149–163

Bayliss A, Volpert V (2015) Patterns for competing populations with species specific nonlocal coupling. Math Model Nat Phenom 10(6):30–47

Bertness MD (1984) Ribbed mussels and *Spartina alterniflora* production in a New England salt marsh. Ecology 65:1794–1807

Bertness MD, Callaway R (1994) Positive interactions in communities. Trends Ecol Evol 9(5):191–193

Bertness MD, Grosholz E (1985) Population dynamics of the ribbed mussel, *Geukensia demissa*: the costs and benefits of an aggregated distribution. Oecologia 67(2):192–204

Billingham J (2003) Dynamics of a strongly nonlocal reaction–diffusion population model. Nonlinearity 17(1):313

Borgogno F, D'Odorico P, Laio F, Ridolfi L (2009) Mathematical models of vegetation pattern formation in ecohydrology. Rev Geophys 47(1):RG1005

Bouma T, Van Duren L, Temmerman S, Claverie T, Blanco-Garcia A, Ysebaert T, Herman PMJ (2007) Spatial flow and sedimentation patterns within patches of epibenthic structures: combining field, flume and modelling experiments. Cont Shelf Res 27(8):1020–1045

Bouma T, Friedrichs M, Van Wesenbeeck B, Temmerman S, Graf G, Herman PMJ (2009) Density-dependent linkage of scale-dependent feedbacks: a flume study on the intertidal macrophyte *Spartina anglica*. Oikos 118(2):260–268

Bouma T, Temmerman S, van Duren L, Martini E, Vandenbruwaene W, Callaghan D, Balke T, Biermans G, Klaassen P, van Steeg P et al (2013) Organism traits determine the strength of scale-dependent bio-geomorphic feedbacks: a flume study on three intertidal plant species. Geomorphology 180:57–65

Britton N (1990) Spatial structures and periodic travelling waves in an integro-differential reaction–diffusion population model. SIAM J Appl Math 50(6):1663–1688

Castets V, Dulos E, Boissonade J, De Kepper P (1990) Experimental evidence of a sustained standing Turing-type nonequilibrium chemical pattern. Phys Rev Lett 64(24):2953

Chen Y, Kolokolnikov T, Tzou J, Gai C (2015) Patterned vegetation, tipping points, and the rate of climate change. Eur J Appl Math 26(6):945–958

Couteron P, Lejeune O (2001) Periodic spotted patterns in semi-arid vegetation explained by a propagation-inhibition model. J Ecol 89(4):616–628

Dakos V, Kéfi S, Rietkerk M, Van Nes EH, Scheffer M (2011) Slowing down in spatially patterned ecosystems at the brink of collapse. Am Nat 177(6):E153–E166

de Jager M, Weissing FJ, van de Koppel J (2017) Why mussels stick together: spatial self-organization affects the evolution of cooperation. Evol Ecol 31:1–12

Deegan LA, Johnson DS, Warren RS, Peterson BJ, Fleeger JW, Fagherazzi S, Wollheim WM (2012) Coastal eutrophication as a driver of salt marsh loss. Nature 490(7420):388–392

Dhooge A, Govaerts W, Kuznetsov Y, Meijer H, Sautois B (2008) New features of the software Matcont for bifurcation analysis of dynamical systems. Math Comput Model Dyn Syst 14(2):147–175

Dibner R, Doak D, Lombardi E (2015) An ecological engineer maintains consistent spatial patterning, with implications for community-wide effects. Ecosphere 6(9):1–17

D'Odorico P, Laio F, Ridolfi L (2006) Patterns as indicators of productivity enhancement by facilitation and competition in dryland vegetation. J Geophys Res Biogeosci 111(G3):1–7

Fagherazzi S (2014) Coastal processes: storm-proofing with marshes. Nat Geosci 7(10):701–702

Fagherazzi S, Kirwan ML, Mudd SM, Guntenspergen GR, Temmerman S, D'Alpaos A, van de Koppel J, Rybczyk JM, Reyes E, Craft C et al (2012) Numerical models of salt marsh evolution: ecological, geomorphic, and climatic factors. Rev Geophys 50(1):RG1002

Fagherazzi S, Mariotti G, Wiberg P, McGlathery K (2013) Marsh collapse does not require sea level rise. Oceanography 26(3):70–77

Fuentes M, Kuperman M, Kenkre V (2003) Nonlocal interaction effects on pattern formation in population dynamics. Phys Rev Lett 91(15):158104

Gedan KB, Kirwan ML, Wolanski E, Barbier EB, Silliman BR (2011) The present and future role of coastal wetland vegetation in protecting shorelines: answering recent challenges to the paradigm. Clim Change 106(1):7–29

Gierer A, Meinhardt H (1972) A theory of biological pattern formation. Biol Cybern 12(1):30–39

Gleason ML, Elmer DA, Pien NC, Fisher JS (1979) Effects of stem density upon sediment retention by salt marsh cord grass, *Spartina alterniflora* loisel. Estuaries 2(4):271–273

Goodman JE, Wood ME, Gehrels WR (2007) A 17-year record of sediment accretion in the salt marshes of Maine (USA). Mar Geol 242(1–3):109–121

Gourley S, Chaplain MA, Davidson F (2001) Spatio-temporal pattern formation in a nonlocal reaction–diffusion equation. Dyn Syst Int J 16(2):173–192

Green JB, Sharpe J (2015) Positional information and reaction–diffusion: two big ideas in developmental biology combine. Development 142(7):1203–1211

Halpern BS, Silliman BR, Olden JD, Bruno JP, Bertness MD (2007) Incorporating positive interactions in aquatic restoration and conservation. Front Ecol Environ 5(3):153–160

Hardaway CS Jr, Byrne RJ (1999) Shoreline management in Chesapeake Bay. Special report in Applied Marine Science and Ocean Engineering No. 356, Virginia Institute of Marine Science, William & Mary, VA, USA

He Q, Bertness MD, Altieri AH (2013) Global shifts towards positive species interactions with increasing environmental stress. Ecol Lett 16(5):695–706

Hiscock TW, Megason SG (2015) Mathematically guided approaches to distinguish models of periodic patterning. Development 142(3):409–419

Kéfi S, Guttal V, Brock WA, Carpenter SR, Ellison AM, Livina VN, Seekell DA, Scheffer M, van Nes EH, Dakos V (2014) Early warning signals of ecological transitions: methods for spatial patterns. PLoS ONE 9(3):e92097

Kéfi S, Holmgren M, Scheffer M (2016) When can positive interactions cause alternative stable states in ecosystems? Funct Ecol 30(1):88–97

Klausmeier CA (1999) Regular and irregular patterns in semiarid vegetation. Science 284(5421):1826–1828

Liu Q-X, Weerman EJ, Herman PMJ, Olff H, van de Koppel J (2012) Alternative mechanisms alter the emergent properties of self-organization in mussel beds. Proc R Soc Lond B Biol Sci 279:rspb20120157

Liu Q-X, Herman PMJ, Mooij WM, Huisman J, Scheffer M, Olff H, van de Koppel J (2014) Pattern formation at multiple spatial scales drives the resilience of mussel bed ecosystems. Nat Commun 5:5234

Madzvamuse A, Ndakwo HS, Barreira R (2015) Cross-diffusion-driven instability for reaction–diffusion systems: analysis and simulations. J Math Biol 70(4):709–743

Mariotti G, Fagherazzi S (2010) A numerical model for the coupled long-term evolution of salt marshes and tidal flats. J Geophys Res Earth Surf 115(F1):F01004

Martínez-García R, Lopez C (2018) From scale-dependent feedbacks to long-range competition alone: a short review on pattern-forming mechanisms in arid ecosystems. Preprint arXiv:1801.01399

Martínez-García R, Calabrese JM, Hernández-García E, López C (2013) Vegetation pattern formation in semiarid systems without facilitative mechanisms. Geophys Res Lett 40(23):6143–6147

Martínez-García R, Calabrese JM, Hernández-García E, López C (2014) Minimal mechanisms for vegetation patterns in semiarid regions. Philos Trans R Soc A Math Phys Eng Sci 372(2027):20140068

Merchant SM, Nagata W (2011) Instabilities and spatiotemporal patterns behind predator invasions with nonlocal prey competition. Theor Popul Biol 80(4):289–297

Möller I, Kudella M, Rupprecht F, Spencer T, Paul M, Van Wesenbeeck BK, Wolters G, Jensen K, Bouma TJ, Miranda-Lange M et al (2014) Wave attenuation over coastal salt marshes under storm surge conditions. Nat Geosci 7(10):727

Murray JD (2001) Mathematical biology. II spatial models and biomedical applications (Interdisciplinary applied mathematics), vol 18. Springer, New York

Nakamasu A, Takahashi G, Kanbe A, Kondo S (2009) Interactions between zebrafish pigment cells responsible for the generation of Turing patterns. Proc Natl Acad Sci 106(21):8429–8434

Ninomiya H, Tanaka Y, Yamamoto H (2017) Reaction, diffusion and non-local interaction. J Math Biol 75(5):1203–1233

Nyman JA, DeLaune RD, Roberts HH, Patrick W Jr (1993) Relationship between vegetation and soil formation in a rapidly submerging coastal marsh. Mar Ecol Prog Ser 96:269–279

Parshad RD, Kumari N, Kasimov AR, Abderrahmane HA (2014) Turing patterns and long-time behavior in a three-species food-chain model. Math Biosci 254:83–102

Perry JE, Atkinson RB (2009) York river tidal marshes. J Coast Res 57:40–49

Priestas AM, Mariotti G, Leonardi N, Fagherazzi S (2015) Coupled wave energy and erosion dynamics along a salt marsh boundary, Hog Island Bay, Virginia, USA. J Mar Sci Eng 3(3):1041–1065

Pringle RM, Tarnita C (2017) Spatial self-organization of ecosystems: integrating multiple mechanisms of regular-pattern formation. Ann Rev Entomol 62(1):359–377

Raspopovic J, Marcon L, Russo L, Sharpe J (2014) Digit patterning is controlled by a Bmp-Sox9-Wnt Turing network modulated by morphogen gradients. Science 345(6196):566–570

Rietkerk M, van de Koppel J (2008) Regular pattern formation in real ecosystems. Trends Ecol Evol 23(3):169–175

Rosen PS (1980) Erosion susceptibility of the Virginia Chesapeake Bay shoreline. Mar Geol 34(1–2):45–59

Rovinsky AB, Menzinger M (1993) Self-organization induced by the differential flow of activator and inhibitor. Phys Rev Lett 70(6):778

Schile LM (2014) Modeling tidal marsh distribution with sea-level rise: evaluating the role of vegetation, sediment, and upland habitat in marsh resiliency. PLoS ONE 9(2):e88760

Schwarz C, Bouma T, Zhang L, Temmerman S, Ysebaert T, Herman PMJ (2015) Interactions between plant traits and sediment characteristics influencing species establishment and scale-dependent feedbacks in salt marsh ecosystems. Geomorphology 250:298–307

Sheehan MR, Ellison JC (2015) Tidal marsh erosion and accretion trends following invasive species removal, Tamar estuary, Tasmania. Estuar Coast Shelf Sci 164:46–55

Shi J, Xie Z, Little K (2011) Cross-diffusion induced instability and stability in reaction–diffusion systems. J Appl Anal Comput 1(1):95–119

Siebert J, Schöll E (2015) Front and Turing patterns induced by Mexican-hat-like nonlocal feedback. Europhys Lett (EPL) 109(4):40014

Siero E, Doelman A, Eppinga M, Rademacher J D, Rietkerk M, Siteur K (2015) Striped pattern selection by advective reaction–diffusion systems: resilience of banded vegetation on slopes. Chaos Interdiscip J Nonlinear Sci 25(3):036411

Silliman BR, van de Koppel J, McCoy MW, Diller J, Kasozi GN, Earl K, Adams PN, Zimmerman AR (2012) Degradation and resilience in louisiana salt marshes after the BP-Deepwater Horizon oil spill. Proc Natl Acad Sci 109(28):11234–11239

Silliman BR, Schrack E, He Q, Cope R, Santoni A, van der Heide T, Jacobi R, Jacobi M, van de Koppel J (2015) Facilitation shifts paradigms and can amplify coastal restoration efforts. Proc Natl Acad Sci 112(46):14295–14300

Stumpf RP (1983) The process of sedimentation on the surface of a salt marsh. Estuar Coast Shelf Sci 17(5):495–508

Tonelli M, Fagherazzi S, Petti M (2010) Modeling wave impact on salt marsh boundaries. J Geophys Res Oceans. https://doi.org/10.1029/2009jc006026

Turing AM (1952) The chemical basis of morphogenesis. Philos Trans R Soc Lond B Biol Sci 237(641):37–72

van de Koppel J, Herman PMJ, Thoolen P, Heip CH (2001) Do alternate stable states occur in natural ecosystems? Evidence from a tidal flat. Ecology 82(12):3449–3461

van de Koppel J, Rietkerk M, Dankers N, Herman PMJ (2005a) Scale-dependent feedback and regular spatial patterns in young mussel beds. Am Nat 165(3):E66–E77

van de Koppel J, van der Wal D, Bakker JP, Herman PMJ (2005b) Self-organization and vegetation collapse in salt marsh ecosystems. Am Nat 165(1):E1–E12

van der Heide T, Eklöf JS, van Nes EH, van der Zee EM, Donadi S, Weerman EJ, Olff H, Eriksson BK (2012) Ecosystem engineering by seagrasses interacts with grazing to shape an intertidal landscape. PLoS ONE 7(8):e42060

Van Hulzen J, Van Soelen J, Bouma T (2007) Morphological variation and habitat modification are strongly correlated for the autogenic ecosystem engineer *Spartina anglica* (common cordgrass). Estuar Coasts 30(1):3–11

van Wesenbeeck BK, van de Koppel J, Herman PMJ, Bouma TJ (2008) Does scale-dependent feedback explain spatial complexity in salt-marsh ecosystems? Oikos 117(1):152–159

Vandenbruwaene W, Temmerman S, Bouma T, Klaassen P, De Vries M, Callaghan D, Van Steeg P, Dekker F, Van Duren L, Martini E et al (2011) Flow interaction with dynamic vegetation patches: implications for biogeomorphic evolution of a tidal landscape. J Geophys Res Earth Surf. https://doi.org/10.1029/2010JF001788

Watt C, Garbary DJ, Longtin C (2010) Population structure of the ribbed mussel *Geukensia demissa* in salt marshes in the southern gulf of St. Lawrence, Canada. Helgol Mar Res 65(3):275

White K (1998) Spatial heterogeneity in three species, plant–parasite–hyperparasite, systems. Philos Trans R Soc B Biol Sci 353(1368):543

Yang W, Wang Q, Pan X, Li B et al (2014) Estimation of the probability of long-distance dispersal: stratified diffusion of *Spartina alterniflora* in the Yangtze river estuary. Am J Plant Sci 5(24):3642

Ysebaert T, Yang S-L, Zhang L, He Q, Bouma TJ, Herman PMJ (2011) Wave attenuation by two contrasting ecosystem engineering salt marsh macrophytes in the intertidal pioneer zone. Wetlands 31(6):1043–1054

Zaytseva S, Shaw LB, Lipcius RN, Shi J, Kirwan ML (2018) Pattern formation in marsh ecosystems modeled through the interaction of marsh vegetation, mussels and sediment. Manuscript in preparation